ADVANCED ENERGY MATERIALS
www.advenergymat.de

Interfacial Oxide Formation Limits the Photovoltage of α-$SnWO_4$/NiO_x Photoanodes Prepared by Pulsed Laser Deposition

*Patrick Schnell, Moritz Kölbach, Markus Schleuning, Keisuke Obata, Rowshanak Irani, Ibbi Y. Ahmet, Moussab Harb, David E. Starr, Roel van de Krol, and Fatwa F. Abdi**

α-$SnWO_4$ is a promising metal oxide photoanode material for direct photoelectrochemical water splitting. With a band gap of 1.9 eV, it ideally matches the requirements as a top absorber in a tandem device theoretically capable of achieving solar-to-hydrogen (STH) efficiencies above 20%. It suffers from photoelectrochemical instability, but NiO_x protection layers have been shown to help overcome this limitation. At the same time, however, such protection layers seem to reduce the photovoltage that can be generated at the solid/electrolyte junction. In this study, an extensive analysis of the α-$SnWO_4$/NiO_x interface is performed by synchrotron-based hard X-ray photoelectron spectroscopy (HAXPES). NiO_x deposition introduces a favorable upwards band bending, but also oxidizes Sn^{2+} to Sn^{4+} at the interface. By combining the HAXPES data with open circuit potential (OCP) analysis, density functional theory (DFT) calculations, and Monte Carlo-based photoemission spectra simulation, the presence of a thin oxide layer at the α-$SnWO_4$/NiO_x interface is suggested and shown to be responsible for the limited photovoltage. Based on this new-found understanding, suitable mitigation strategies can be proposed. Overall, this study demonstrates the complex nature of solid-state interfaces in multi-layer photoelectrodes, which needs to be unraveled to design efficient heterostructured photoelectrodes for solar water splitting.

1. Introduction

In order to establish a clean and sustainable future energy supply, significant research efforts have been devoted to developing novel renewable energy technologies. Sunlight is the most abundant renewable energy source, but its availability is limited by the diurnal and seasonal cycles. To overcome this, solar energy can be photoelectrochemically converted into hydrogen,[1,2] which can be stored and used directly as fuel or used as a feedstock to synthesize other chemical fuels.[3–5] Metal oxide semiconductors have been considered as viable photoelectrode materials for direct photoelectrochemical water splitting.[6,7] They are generally more stable in aqueous media and easier to process than conventional semiconductors.[8,9] The semiconducting properties, such as carrier transport, are rather poor (compared to, e.g., III–V[10–12] semiconductors or Si[13]), but various strategies have been proposed to at least partially overcome this (e.g., doping, nanostructuring, overlayer deposition).[14–16] Using these strategies photocurrents close to the theoretical maximum have been demonstrated for $BiVO_4$ photoelectrodes, establishing $BiVO_4$ as one of the highest performing metal oxide photoabsorbers.[15] This means that the performance of $BiVO_4$ is no longer limited by its quantum efficiency, but by its relatively large bandgap (≈2.4 eV) and the photovoltage losses in the material.

Another metal oxide candidate is α-$SnWO_4$. There are currently only a few comprehensive studies available on this material, but the reported properties are promising.[17–24] It is an n-type semiconductor with an indirect band gap of 1.9 eV,[17] implying a theoretical maximum photocurrent of up to ≈17 mA cm^{-2} under AM 1.5 solar irradiation. Another attractive property of this material is the flat band potential which is located at ≈0 V versus the reversible hydrogen electrode potential (RHE).[22–24] To date, α-$SnWO_4$ thin film photoelectrodes have been prepared successfully using various techniques, including hydrothermal conversion,[19,23] magnetron sputtering,[20–22] and pulsed laser deposition (PLD).[17,18] A major challenge with this material is the limited stability due to surface oxidation of Sn^{2+} to Sn^{4+} under (photo)electrochemical

P. Schnell, Dr. M. Kölbach, M. Schleuning, Dr. K. Obata, Dr. R. Irani, Dr. I. Y. Ahmet, Dr. D. E. Starr, Prof. R. van de Krol, Dr. F. F. Abdi
Institute for Solar Fuels
Helmholtz-Zentrum Berlin für Materialien und Energie GmbH
Hahn-Meitner-Platz 1, Berlin 14109, Germany
E-mail: fatwa.abdi@helmholtz-berlin.de
P. Schnell, Prof. R. van de Krol
Institut für Chemie
Technische Universität Berlin
Straße des 17. Juni 124, Berlin 10623, Germany
Dr. M. Harb
KAUST Catalysis Center (KCC)
Physical Sciences and Engineering Division (PSE)
King Abdullah University of Science and Technology (KAUST)
Thuwal 23955-6900, Saudi Arabia
The ORCID identification number(s) for the author(s) of this article can be found under https://doi.org/10.1002/aenm.202003183.

DOI: 10.1002/aenm.202003183

conditions, which presumably results in the formation of an SnO_2 surface layer. This layer blocks charge transport and limits the photocurrent, but it also protects the material from further corrosion (self-passivation). Interestingly, the formation of this blocking layer can be (partially) suppressed by the deposition of a 20 nm NiO_x protection layer using PLD.[17] This improves the photocurrent, resulting in a record value of 0.75 mA cm^{-2} for sulfite oxidation at 1.23 V versus RHE, while still showing good stability.

The improved photocurrent, however, is accompanied by a reduction of the photovoltage, as suggested by the shift in the photocurrent onset potential and the smaller difference in open circuit potential (ΔOCP) between dark and light conditions. We tentatively attributed these limitations to possible Fermi-level pinning at the α-$SnWO_4/NiO_x$ interface, but have not yet been able to show direct evidence for this. In the present study, we provide a detailed fundamental systematic investigation of the α-$SnWO_4/NiO_x$ interface. Synchrotron-based hard X-ray photoelectron spectroscopy (HAXPES) is used to reveal depth-dependent information about the chemical states and the electronic structure at the α-$SnWO_4/NiO_x$ interface. The HAXPES data are complemented with ΔOCP analysis, density functional theory (DFT) calculations, and Monte Carlo-based photoemission peak intensity simulation. Based on this comprehensive analysis we are able to unravel the origin of the limitation at the α-$SnWO_4/NiO_x$ interface and propose suitable mitigation strategies.

2. Results and Discussion

We first verify that the NiO_x protection layer limits the photovoltage of α-$SnWO_4$ by performing a series of ΔOCP measurements. A series of 100 nm-thick phase-pure α-$SnWO_4$ films (see Figure S1, Supporting Information, for a representative X-ray diffractogram) deposited on FTO were coated with varying thicknesses of NiO_x, using our previously published PLD procedure.[17,18] **Figure 1** shows the ΔOCP for a pristine α-$SnWO_4$ film and α-$SnWO_4$ films coated with increasing thicknesses of NiO_x measured in a 0.5 M KP_i + 0.5 M Na_2SO_3 electrolyte at pH ≈7.2. The Na_2SO_3 served as a hole scavenger. A continuous decrease in ΔOCP is observed with increasing NiO_x thickness up to 10 nm, beyond which the ΔOCP saturates at ≈0.1 V. This confirms our previous observation[17] and suggests that the underlying mechanism of the photovoltage limitation is related to a modification of the $SnWO_4/NiO_x$ interface upon deposition of NiO_x.

A reduction of photovoltage in metal oxides is often correlated with the presence of intraband states,[25,26] which may arise from the formation of hydroxide or oxyhydroxide species at the surface, for instance as a result of air-exposure. Our previously established procedure includes exposing the α-$SnWO_4$ films to air prior to NiO_x deposition; the films were taken out of the PLD chamber to a separate Ar annealing furnace and reintroduced back into the PLD chamber for NiO_x deposition. To evaluate whether this may be the underlying reason for the photovoltage losses, an alternative preparation process was developed where all deposition and annealing steps are performed within the PLD system (i.e., no air-exposure). Although the dark currents vary, films prepared using both procedures show the same photocurrent and relatively high onset potential (see Figure S2, Supporting Information, for chopped linear sweep voltammetry), suggesting that air-exposure is not the origin for the photovoltage losses at the α-$SnWO_4/NiO_x$ interface.

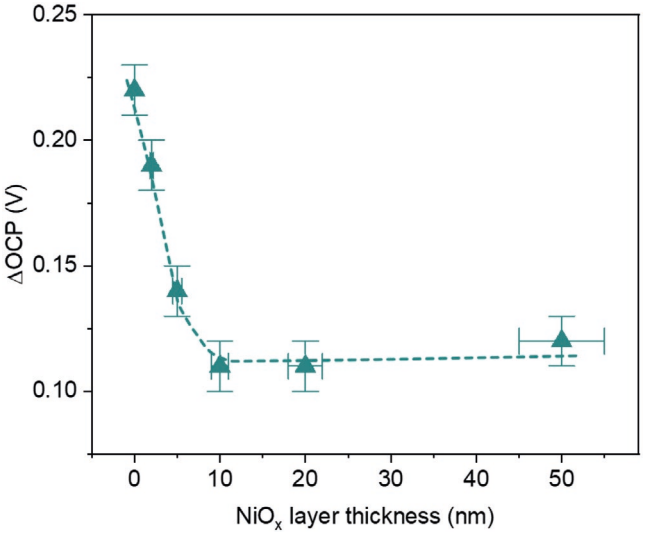

Figure 1. Difference of open circuit potential between AM1.5 illumination and dark (ΔOCP) for a pristine α-$SnWO_4$ and for films coated with different PLD NiO_x layer thicknesses. A decrease of the ΔOCP from 0.22 V (pristine film) to ≈0.1 V can be observed which saturates after deposition of NiO_x thicker than 10 nm. Measurements were performed in 0.5 M KP_i with 0.5 M Na_2SO_3 added as hole scavenger at pH ≈7.2. For the NiO_x thickness an error of 10% was estimated from the deposition rate calibration.

A detailed investigation of the chemical states and electronic structure of the α-$SnWO_4/NiO_x$ interface was performed using synchrotron-based HAXPES. Such a study will help to identify the root cause of the interfacial losses and propose appropriate improvement strategies. Our experimental approach is depicted in **Figure 2**.

In brief, similar to the ΔOCP measurements, we varied the NiO_x layer thickness (between 0 and 50 nm) deposited on the 100 nm α-$SnWO_4$ film. As the NiO_x thickness increases, the photoelectron signal originating from α-$SnWO_4$ is increasingly attenuated until only photoelectrons escaping from the NiO_x layer are detected. This allows us to de-convolute the interfacial spectral features from those arising from the bulk and/or the surface. In addition, depth-dependent information is further gained by varying the kinetic energy of the incident photons ($h\nu$) between 2, 4, and 6 keV. The respective probing depths, σ, for these different photon energies correspond to three times the inelastic mean free path, λ, and are indicated in Figure 2.

Before we discuss the effect of NiO_x deposition in detail, the chemical states of pristine α-$SnWO_4$ films are first evaluated. W 4f and Sn 3d core level spectra of a pristine α-$SnWO_4$ film measured with $h\nu = 2$ keV are shown in **Figure 3**a,b, respectively. The W 4f core level spectrum can be deconvoluted into two contributions (Figure 3a, see Experimental Section for the fitting procedure). W^{6+} is mainly present as expected for α-$SnWO_4$, and a minor contribution of W^{5+} is also detected. We confirm that the existence of W^{5+} is not related to beam damage (as is known for WO_3[27]), as shown from our measurements with different beam filters and at different sample spots (see Figure S3, Supporting Information, for details). The contribution of W^{5+} to the

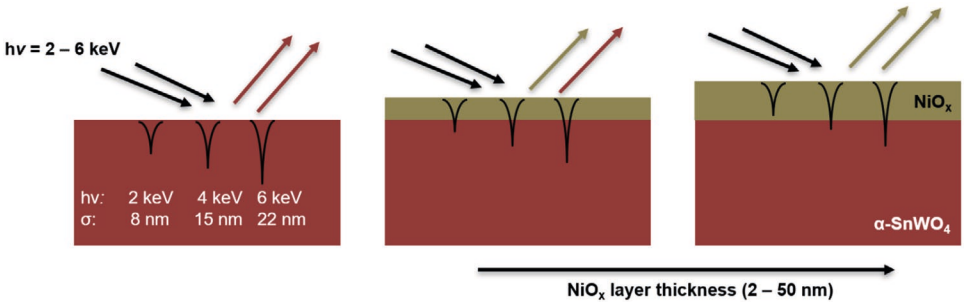

Figure 2. Schematic illustration of our HAXPES interface experiment. α-$SnWO_4$ films are coated with a NiO_x layer with increasing thickness such that the interfacial spectral features can be deconvoluted from features arising from the bulk and the surface. The kinetic energy of photons ($h\nu$) is varied between 2, 4, and 6 keV. The increasing probing depth σ, which is equal to three times the inelastic mean free path λ, for the different photon energies is indicated. The brown arrows depict the excited photoelectrons from α-$SnWO_4$, while the excited photoelectrons from NiO_x are illustrated with the clay creek arrows.

total signal increases with increasing photon energy $h\nu$, which corresponds to increasing probing depth σ (see Figure 3c; the spectra are shown in Figure S4a, Supporting Information). This suggests that W^{5+} is present more in the bulk than at the surface of the film. We note that W^{5+} was not observed in the lab-based X-ray photoelectron spectroscopy (XPS) spectra of our previously reported α-$SnWO_4$,[17] whereas the same lab-based XPS measurement for our current sample does reveal the presence of W^{5+}. Since samples produced both in the previous and current work have very similar ΔOCP and photocurrent onset potential, we confirm that the presence of W^{5+} has no impact on these parameters, which are the metrics of interest investigated here. The exact origin of the W^{5+} contribution observed in the present study is not fully clear at this point and while the presence of W^{5+} is undoubtedly interesting—for example, to investigate the influence on the charge transport properties—it is not the main motivation of the present study. The Sn 3d core level spectrum (Figure 3b) shows the presence of mainly Sn^{2+} with a small contribution of oxidized Sn^{4+}. For $h\nu = 2$ keV, the relative contribution of Sn^{4+} to the total signal is estimated to be 18 ± 3%, which is in the same range as measured previously with lab-based photoelectron spectroscopy ($h\nu = 1486.74$ eV).[17] In contrast to W^{5+}, the relative contribution of Sn^{4+} tends to decrease with increasing probing depths σ (Figure 3c; see Figure S4b, Supporting Information, for the spectra). This indicates that the relative contribution of Sn^{4+} is higher at the surface of α-$SnWO_4$ than in the bulk of the material, which makes it relevant for our interface study. Finally, we note that the binding energies do not shift with varying photon energies (see Figure S4, Supporting Information), indicating that no significant band bending is present at the surface of pristine α-$SnWO_4$ films under the HAXPES measurement conditions.

The influence of the NiO_x film on the α-$SnWO_4/NiO_x$ interface is now evaluated by considering the evolution of the W 4f and Sn 3d core level spectra with increasing NiO_x thickness. **Figure 4**a shows the W 4f core level spectra for $SnWO_4$ films coated with different NiO_x layer thicknesses, measured with $h\nu = 2$ keV (see Figures S6–S8, Supporting Information, for fitted spectra, also at different photon energies). The W^{6+} peaks show a clear shift to lower binding energies with increasing NiO_x thickness (see vertical red dashed line in Figure 4a). A detailed discussion on this will follow later. The contribution of W^{5+} is still clearly present for films with NiO_x thickness up to 10 nm and the position of the peak (i.e., binding energy) remains relatively constant independent of the photon energy (see Figure 4c and the vertical orange dashed line at 33.8 eV in Figure 4a). For thicknesses larger than 10 nm the relative W^{5+} contribution seems to decrease, although the poor signal-to-noise ratio precludes a quantitative evaluation. This trend is especially true for the data obtained using higher photon energies (i.e., 4 and 6 keV, see Figure 4c), which agrees very well with the notion that W^{5+} is present more in the bulk versus at the surface/interface.

In the following, the influence of the NiO_x thickness on the Sn 3d core level spectra (Figure 4b) is evaluated. All spectra can be de-convoluted into Sn^{2+} and Sn^{4+} contributions (see Figures S9–S11, Supporting Information). The relative Sn^{4+} contribution increases with increasing NiO_x layer thickness (Figure 4d), and for a photon energy of 2 keV, Sn^{4+} becomes the dominant oxidation state (>50%) when the NiO_x thickness is ≥10 nm. The increasing contribution of Sn^{4+} is also apparent from the shifts of the peak maxima towards higher binding energies (Figure 4b). We note that this trend qualitatively correlates with the trend of ΔOCP shown in Figure 1, that is, the ΔOCP starts to saturate at the same NiO_x layer thickness when Sn^{4+} starts to dominate the HAXPES signal. The same trend is observed for the different photon energies (Figure 4d), but the higher photon energies (i.e., higher probing depths) show a smaller increase of the relative Sn^{4+} contribution with increasing NiO_x thickness. This indicates that the oxidation of Sn occurs at the α-$SnWO_4/NiO_x$ interface and not in the bulk of α-$SnWO_4$. The influence of the increasing contribution of Sn^{4+} on the interface properties and the photovoltage will be discussed in more detail below.

The O1s core level spectra measured with different photon energies can be found in Figures S12–S14, Supporting Information. The ratios between peaks arising from oxygen in α-$SnWO_4$ and NiO_x (at higher and lower binding energies, respectively) change in the expected manner with the NiO_x thickness and the photon energy $h\nu$. The Ni 2p core level spectra do not change significantly for different NiO_x layer thicknesses, independent of the photon energy (see Figures S12-S15, Supporting Information). This indicates that the chemical nature of NiO_x remains the same with increasing thickness. The valence band (VB) spectra were recorded as well and can be seen in Figure S16,

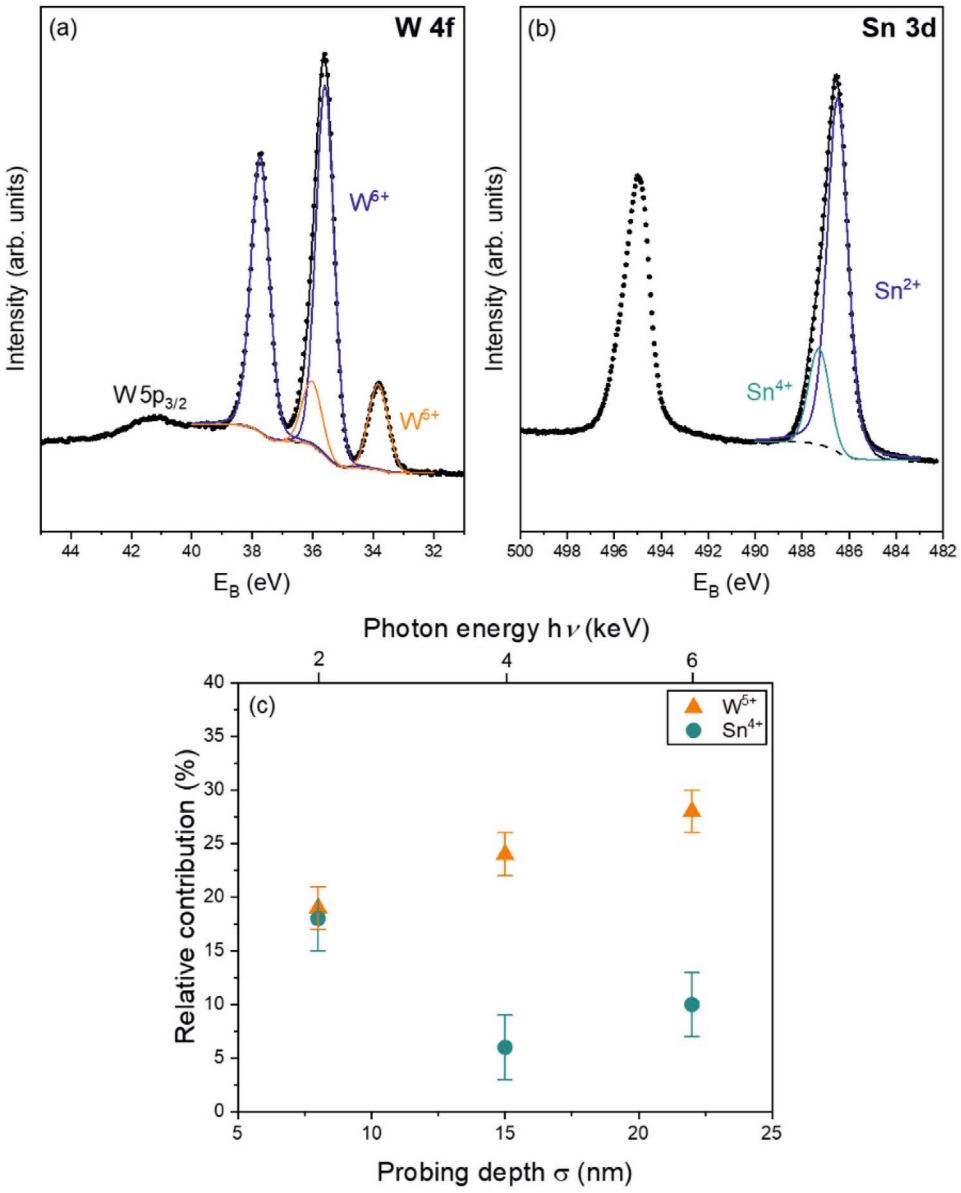

Figure 3. a) W 4f and b) Sn 3d core level photoemission spectra for pristine α-$SnWO_4$ films measured with $h\nu = 2$ keV. A contribution of reduced W^{5+} can be observed in W 4f core levels in addition to W^{6+} corresponding to nominal α-$SnWO_4$. In Sn 3d core levels a small contribution of oxidized Sn^{4+} differing from nominal Sn^{2+} can be found as indicated by the peak asymmetry towards higher binding energy. c) Relative W^{5+} and Sn^{4+} contributions to the total W 4f and Sn 3d signals, respectively, as a function of photon energy, extracted by peak fitting (the spectra are shown in Figure S4, Supporting Information). The probing depth σ corresponds to three times the inelastic mean free path λ at each particular kinetic energy.

Supporting Information, with features of the α-$SnWO_4$ VB becoming smaller, as expected, with increasing NiO_x thickness.

We note that our ability to still detect photoelectrons from the W 4f and Sn 3d core levels for the thicker NiO_x films (>10 nm) seems inconsistent with the expected probing depth of the photon energies used. This is because the NiO_x films are not flat and dense, but instead exhibit island-type growth, as already shown by the scanning electron micrographs in our earlier publication.[17]

The binding energies for different peaks extracted from fitting the W $4f_{7/2}$ and Sn $3d_{5/2}$ core level spectra are shown in **Figure 5** as a function of the NiO_x layer thickness (see Figures S6–S11, Supporting Information, for fitted spectra). The data for the different oxidation states (i.e., W^{5+}, W^{6+}, Sn^{2+}, Sn^{4+}) are shown separately. A shift of ≈0.4 eV towards lower binding energies is observed for W^{6+}. In contrast, as already mentioned above, NiO_x deposition has no significant impact on the binding energies of W^{5+}. The Sn $3d_{5/2}$ peaks also experience a shift towards lower binding energies and saturate after the deposition of 10 nm NiO_x. Both Sn^{2+} and Sn^{4+} peaks experience the same ≈0.4 eV shift that is observed for the W^{6+} peak.

We attribute the correlated shift in the binding energies of W^{6+}, Sn^{2+}, and Sn^{4+} to an electronic shift and a change in band bending in α-$SnWO_4$ as a result of NiO_x deposition. A shift to

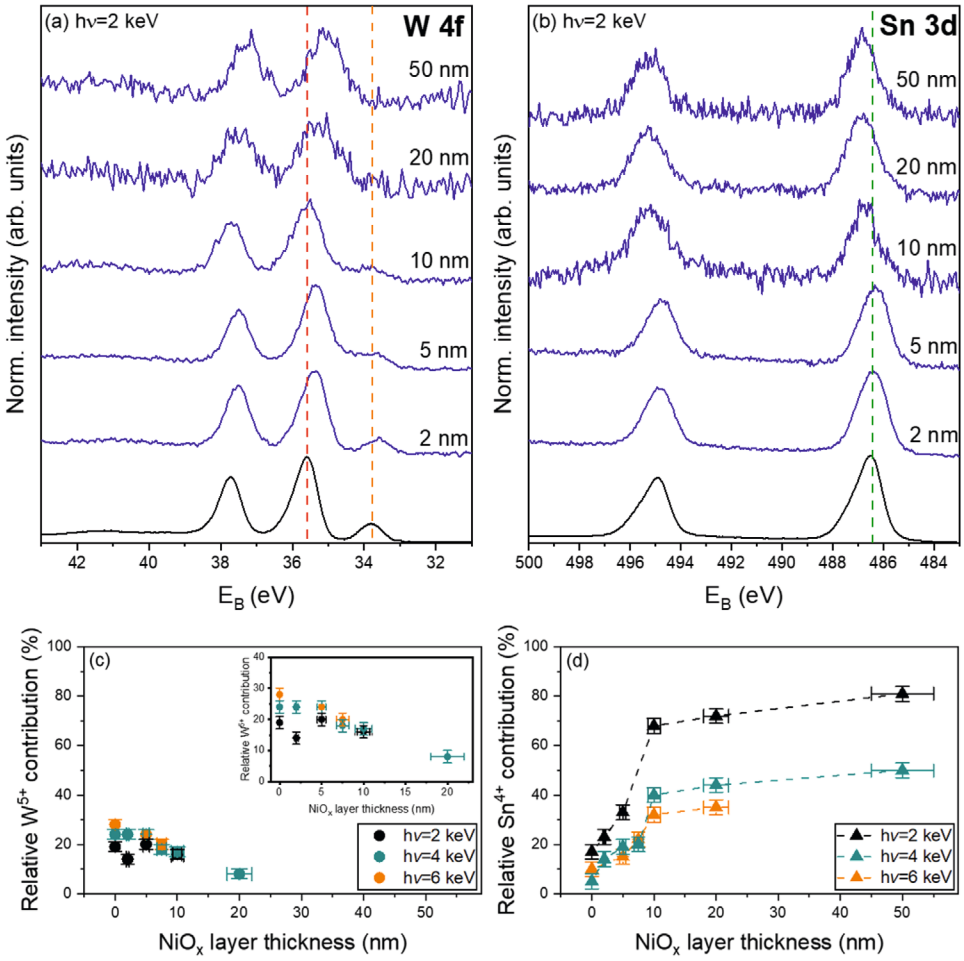

Figure 4. a) W 4f and b) Sn 3d core level spectra measured with $h\nu = 2$ keV for a pristine α-$SnWO_4$ film (black) and films coated with increasing NiO_x layer thickness (blue). The dashed vertical lines indicate the binding energies of the W^{5+} (red), W^{6+} (orange), and Sn^{2+} (dark cyan) of the pristine α-$SnWO_4$ film. O 1s, Ni 2p, and valence band spectra can be found in Figures S12–S16, Supporting Information, and the W 4f and Sn 3d spectra measured with higher $h\nu$ are shown in Figure S5, Supporting Information. c) The relative W^{5+} contribution to the total signal in dependence on the NiO_x layer thickness seems to decrease, especially based on the data obtained using 4 and 6 keV photon energies (see inset), although the poor signal-to-noise ratio prevents a quantitative analysis for samples with thicker NiO_x. The corresponding data points for samples with 20 and 50 nm NiO_x can therefore not be depicted. d) The relative contribution of Sn^{4+} increases with increasing NiO_x layer thickness. The increase of the relative Sn^{4+} contribution is larger for lower $h\nu$ indicating that the oxidation occurs at the interface and not the bulk. For the sample with 50 nm NiO_x a quantitative analysis is not possible for a photon energy of 6 keV due to the poor signal-to-noise ratio.

lower binding energies corresponds to an upward bending of the energy bands (i.e., additional band bending at the surface). At the same time, the Ni 2p binding energies do not shift (see Figures S12–S15, Supporting Information), indicating that the additional band bending is only present in the α-$SnWO_4$ film. Similar observations have been reported in the literature, for instance for $BiVO_4$ deposited with various overlayers[28,29] and metal oxide/Si buried junction photoabsorbers,[30,31] where the observed performance improvement has been attributed to additional band bending. In our case, however, the additional band bending with increasing NiO_x deposition contradicts the decreasing ΔOCP shown in Figure 1. This suggests that a compensating factor is present that negates the favorable effect of band bending. We assign the significant oxidation of Sn^{2+} to Sn^{4+} as the compensating factor that causes the reduction of the photovoltage. The details of this mechanism are discussed in the following paragraphs.

We should point out that the lack of binding energy shift for the W^{5+} peaks seems inconsistent with the band bending explanation above. While the reason for this is not clear at this point, we speculate that it may be caused by one (or a combination) of the following two factors. First, the W^{5+} species may be present in a separate amorphous impurity phase outside of the α-$SnWO_4$ phase. Second, since band bending is a pure interface phenomenon, the peak position of W^{5+}—which is predominantly present in the bulk—is less sensitive to band bending than other species at the interface. We note, however, that the presence of W^{5+} does not affect the limited photovoltage in α-$SnWO_4$ which is the focus of this study.

DFT/HSE06 method calculations were applied to analyze the electronic structure of α-$SnWO_4$ and how this is influenced by the presence of Sn^{4+} defects. We used a similar methodology as has been reported previously for pristine α-$SnWO_4$.[21,22] We took a compensation approach by introducing vacancies in

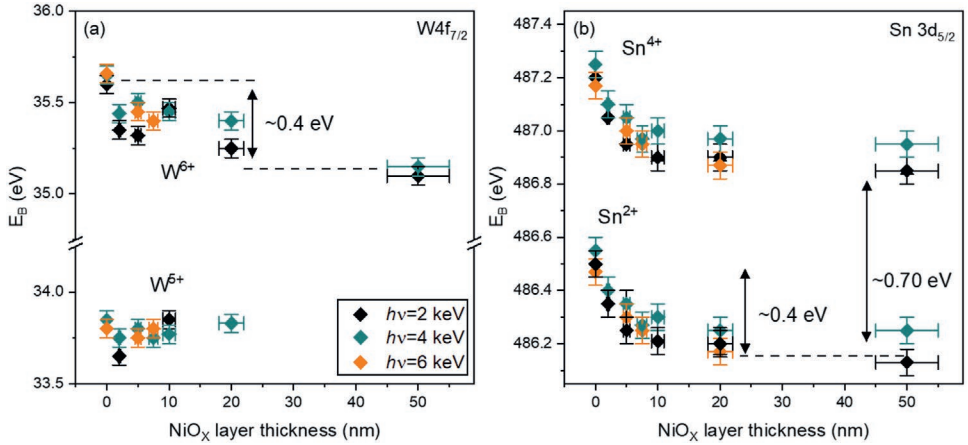

Figure 5. Influence of NiO_x layer thickness on a) W $4f_{7/2}$ and b) Sn $3d_{5/2}$ peak positions measured with different photon energies hν. No shift is observed for W^{5+}, while the W^{6+}, Sn^{2+}, and Sn^{4+} peaks shift to lower binding energies (by up to ≈0.4 eV) with increasing NiO_x layer thickness. This is attributed to upwards band bending in α-$SnWO_4$. All binding energies were determined by the fitting procedure described in the Experimental Section.

order to simulate the presence of Sn^{4+}. Among the explored self-defective structures containing either O-, Sn- or W-vacancies and the structures containing anti-site defects, only the one associated with W-vacancy could represent the possible presence of Sn^{4+} (see Figures S17 and S18, Supporting Information, for more details regarding other structures). **Figure 6**a,b show the orthorhombic crystal structure of pristine α-$SnWO_4$ as well as α-$SnWO_4$ that contains Sn^{4+} defects. The density of states (DOS) plots for these two structures are shown in Figures 6c and 6d. The band gap in α-$SnWO_4$ originates from indirect transitions between the occupied Sn $5s^2$ + O $2p^6$ and the unoccupied W $5d^0$ states. The introduction of Sn^{4+} does not modify the band gap, but it results in the appearance of a narrow state in the middle of the band gap. This state has a highly localized character as revealed by the partial charge density map shown in Figure S19, Supporting Information. Such a mid-gap state is known to be able to pin the Fermi level and therefore restrict the extractable photovoltage.[32,33]

Before making any definite conclusions based on these DFT results, we first critically assess how well the structure in the proposed model represents our α-$SnWO_4$ films. In particular, it has to be examined whether W vacancies, required to compensate the Sn^{4+} defects, actually occur in our α-$SnWO_4$ films. There are three arguments against the presence of W vacancies. First, we observed previously by Rutherford backscattering spectrometry (RBS) that our deposition procedure generally results in slightly W-rich films.[17] Second, based on the compensation model used in the DFT, one would expect a higher value of the Sn/W ratio with increasing NiO_x thickness, that is, more W vacancies due to a higher amount of Sn^{4+}. However, this is inconsistent with our HAXPES data (see Figure S20, Supporting Information). Finally, for electrostatic reasons, a W vacancy is likely to have a high defect formation enthalpy due to the high formal oxidation state of W (6+). All these arguments suggest that it is rather unlikely that a significant amount of W vacancies is present in our samples. Consequently, we conclude that there has to be another mechanism that charge-compensates the Sn^{4+} defects and that may explain the reduced photovoltage.

Another mechanism that may explain the increase of Sn^{4+} is the formation of a secondary phase at the α-$SnWO_4$/NiO_x interface. Although the NiO_x deposition was performed at room temperature, the presence of O_2 plasma during the PLD process may cause the formation of this phase; indeed, a preliminary experiment of intentionally exposing our pristine α-$SnWO_4$ to O_2 plasma resulted in a similar increase of Sn^{4+} contribution. Such a formation of interfacial layer from a secondary phase has been reported in other systems, such as at the Cu_2O/ZTO (zinc-tin-oxide) interface and Si/HfO_2 interface.[34–36] A possible identity of this secondary phase is $Sn_{0.23}WO_3$, which has been reported to be present as impurities in several α-$SnWO_4$ films.[18,37] This is, however, unlikely to be the case. The $Sn_{0.23}WO_3$ phase has been reported to contain Sn^{2+} and Sn^0, but no Sn^{4+}.[38] $Sn(WO_4)_2$ is another possibility, but to the best of our knowledge, this phase has only been reported based on theoretical calculation.[39]

Instead, we speculate that the secondary phase at the α-$SnWO_4$/NiO_x interface is SnO_2. We thus quantitatively assess whether the formation of an SnO_2 layer can be correlated with our HAXPES results by performing Monte Carlo simulations of photoemission peak intensities using the SESSA software package.[40] The simulations were performed for α-$SnWO_4$ films coated with an increasing thickness of SnO_2 at the surface (see Figure S21, Supporting Information, for more details). For simplicity, we do not include the NiO_x layer in the simulations, since it would only attenuate the overall Sn 3d spectrum but not change the relative contribution of Sn^{2+} and Sn^{4+} to the spectra, regardless of where these species are located (surface or bulk).

Figure 7a displays the relative contribution of Sn^{4+} to the total Sn 3d HAXPES signal as a function of NiO_x thickness, as obtained from our experimental data. This data is now compared with the simulated results. For each simulated spectrum of an α-$SnWO_4$ film covered with different SnO_2 layer thicknesses (see Figure S21, Supporting Information), the relative contribution of Sn^{4+} is extracted and shown as a function of the SnO_2 layer thickness in Figure 7b. We combine this simulated data with the experimentally observed relative Sn^{4+} contribution

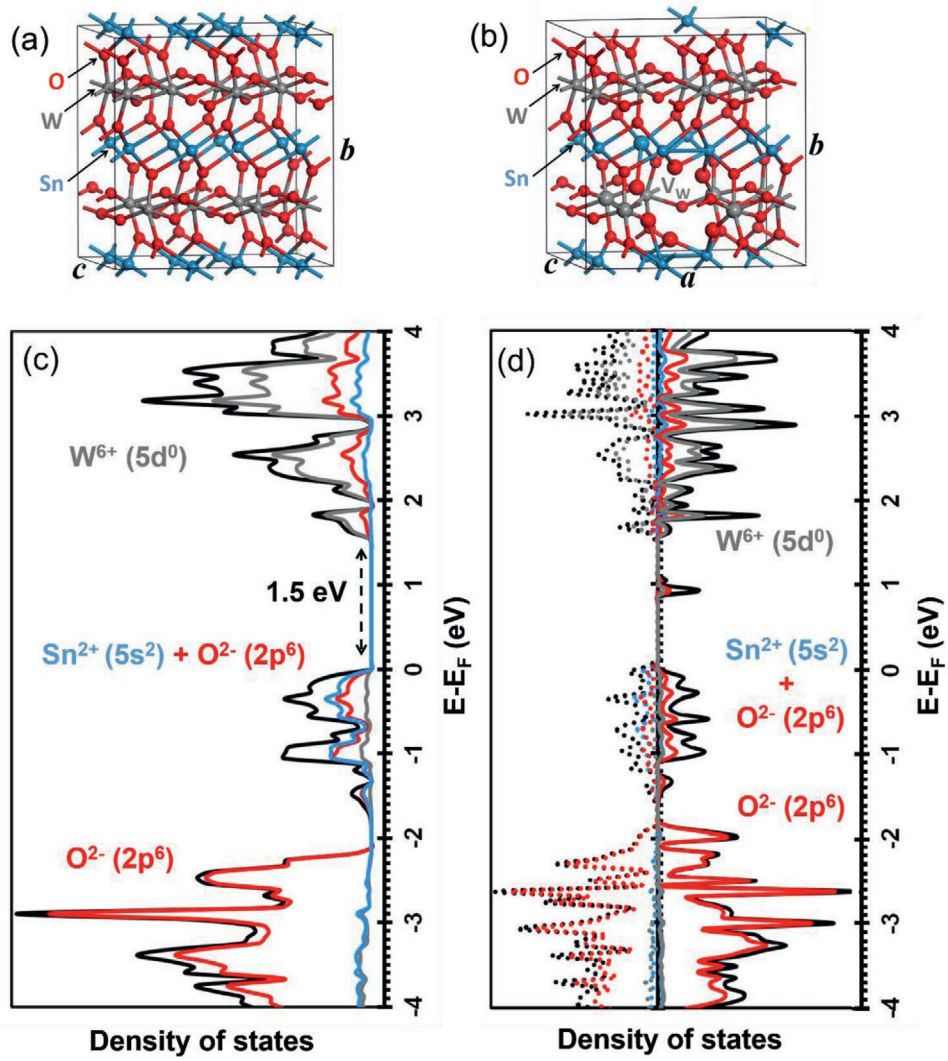

Figure 6. DFT-based orthorhombic crystal lattice of a) pristine α-$SnWO_4$ and b) α-$SnWO_4$ containing W vacancies to compensate Sn^{4+} defects. The corresponding density of states (DOS) is shown in (c) and (d), respectively. In the case where W vacancies are present, the triplet spin state is the most stable configuration; the spin-up (dashed lines) and spin-down (solid lines) components of the DOS are therefore shown.

(Figure 7a) in order to estimate the expected interfacial SnO_2 layer thickness for films with various deposited NiO_x layer thickness. The resulting data is shown in Figure 7c, which clearly shows that a thicker NiO_x layer indeed corresponds to a thicker SnO_2 layer at the interface.

For the sample that shows record photocurrent (i.e., 20 nm thick NiO_x), an interfacial SnO_2 layer thickness of ≈2 nm is estimated. The transmission electron microscope (TEM) image presented in Figure S22, Supporting Information, suggests that such a layer is indeed present at the interface. Although the interfacial layer is thin enough to allow charge carriers to be transferred across the interface (i.e., tunneling), such a layer may negatively affect the α-$SnWO_4/NiO_x$ interface. For example, this insulating layer may limit the extractable photocurrent. An important question relevant to the current study is whether the presence of such a layer can be correlated with the reduced photovoltage. To address this question, ΔOCP measurements were performed again with a pristine α-$SnWO_4$ film, to which different durations of chronoamperometry treatment under AM1.5 illumination at a potential of 1.23 V versus RHE were applied. Since such a treatment has been shown to induce SnO_2 layer formation at the surface of α-$SnWO_4$,[17] the different durations (i.e., different amounts of transferred charges across the interface) would result in different thicknesses of the SnO_2 layer. After each step an OCP measurement was performed. **Figure 8** shows the ΔOCP as a function of the amount of charge transferred across the α-$SnWO_4$ surface (Q), calculated by integrating the chronoamperometry data. The SnO_2 layer thickness on the surface can also be estimated from the amount of charge and the reported density of SnO_2 (7.02 g cm^{-3}),[41] as shown at the top x-axis of the figure (see also Figure S23, Supporting Information, for the cross-section SEM image for the sample with the thickest SnO_2 layer). With increasing Q, the ΔOCP decreases reaching a value of ≈0.08 V. This confirms that the formation of an SnO_2 layer on the surface of α-$SnWO_4$ results in a reduction of the ΔOCP. Based on this observation and the

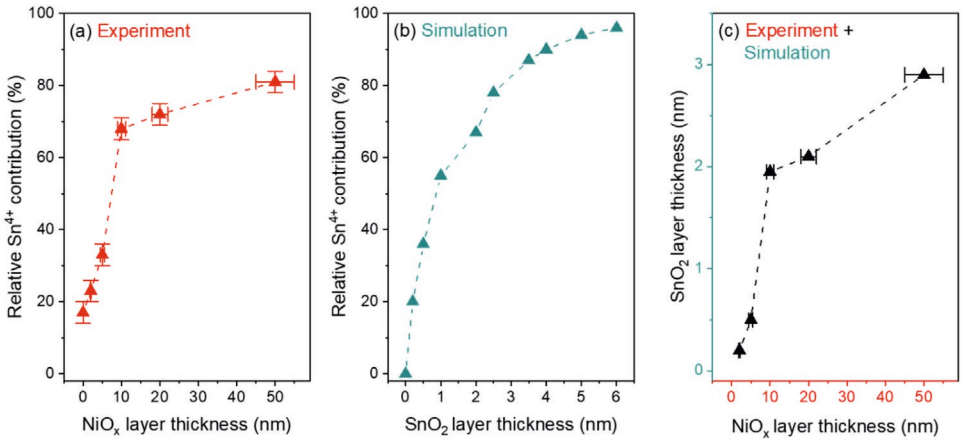

Figure 7. a) Relative Sn^{4+} contribution to the total signal as a function of NiO_x thickness from HAXPES experimental data measured with a photon energy of 2 keV. b) Relative Sn^{4+} contribution to the total signal as a function of SnO_2 layer thickness extracted from Monte Carlo simulation of peak intensities with the SESSA software package, also simulated with a photon energy of 2 keV. c) Correlation of simulation and experimental data. The SnO_2 layer thickness is estimated by using the fraction of Sn^{4+} signal observed experimentally for a given NiO_x thickness and reading the SnO_2 thickness from (a) for that fraction of Sn^{4+} signal (b). For the sample that shows the record photocurrent (i.e., 20 nm thick NiO_x), an interfacial SnO_2 layer thickness of ≈2 nm is estimated.

qualitative agreement with data shown in Figure 1, we conclude that the formation of an interfacial SnO_2 layer at the α-$SnWO_4$/NiO_x interface is responsible for the limited photovoltage that can be extracted.

We finally note that our current findings complement our previous report,[17] where it was mentioned that the hole-induced electrochemical oxidation of Sn^{2+} to Sn^{4+} is prevented by a NiO_x protection layer and a stable photocurrent for at least 0.5 h can be achieved. Our more thorough HAXPES investigation in the present study provides additional understanding on the protection mechanism. PLD NiO_x introduces some oxidation of α-$SnWO_4$ during deposition, but it limits the formed SnO_2 layer thickness such that charge carrier transport is still possible. Furthermore, NiO_x impedes further (photo)electrochemical oxidation of $SnWO_4$, and the formation of a thick hole blocking SnO_2 layer (>7 nm).

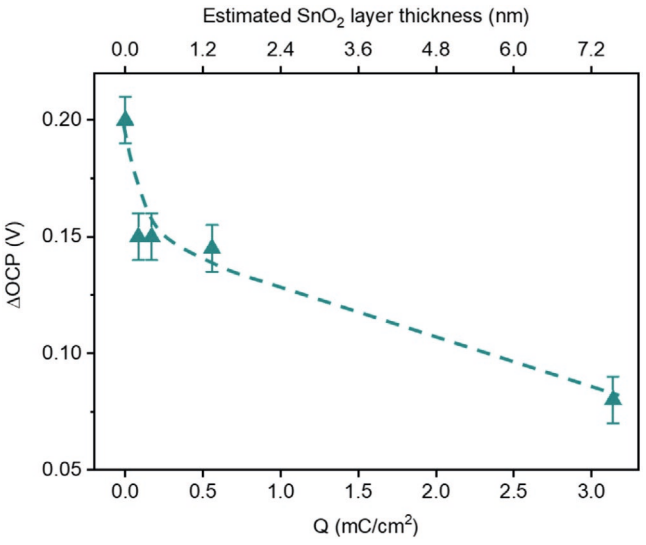

Figure 8. ΔOCP measurements performed on pristine α-$SnWO_4$ after being photoelectrochemically treated at 1.23 V versus RHE for a specific duration. The charge Q was calculated from the recorded chronoamperometry data. The decrease in ΔOCP is correlated with the oxidation of Sn^{2+} to Sn^{4+} and the formation of an SnO_2 layer. The estimated SnO_2 layer thickness on the top x-axis was calculated from the transferred charge Q and the reported density of SnO_2 (7.02 g cm^{-3}).[41] The dashed line is a guide for the eye.

3. Conclusion

In summary, we performed a detailed investigation of the α-$SnWO_4$/NiO_x interface using synchrotron-based HAXPES in order to understand the origin of the limited photovoltage in NiO_x-coated α-$SnWO_4$ films. NiO_x deposition was found to introduce a favorable upwards band bending at the α-$SnWO_4$/NiO_x interface. However, this is accompanied by the oxidation of Sn^{2+} to Sn^{4+}, the degree of which is in a good agreement with the decrease of photovoltage as shown by the open circuit potential (OCP) analysis. Using DFT and Monte Carlo based photoemission intensity simulation, we showed that the increase of Sn^{4+} signal can be explained by the formation of a thin oxide layer, such as SnO_2, at the interface of α-$SnWO_4$ and NiO_x. For the optimized sample with 20 nm-thick NiO_x, an interfacial oxide layer thickness of ≈2 nm is estimated. Although this is in principle thin enough for charge carriers to tunnel through, control experiments by intentionally converting the surface of α-$SnWO_4$ films to an SnO_2 layer with different thicknesses indeed revealed a reduction of the photovoltage in this thickness range. This suggests that the Fermi level pinning is not caused by a direct contact of α-$SnWO_4$ and NiO_x, but is instead related to the presence of the interfacial oxide layer. To overcome the photovoltage limitation, alternative deposition techniques for NiO_x (e.g., vacuum evaporation, atomic layer deposition) or other co-catalyst/protection layers that do not alter the surface of oxidation-sensitive α-$SnWO_4$ need to be explored. This would prevent the formation of the interfacial oxide layer and would enable the extraction of the

maximum photovoltage from the system. Finally, our study shows that understanding the interface properties of metal oxide-based solid-state junctions is paramount in the development of highly efficient and stable electrodes for photoelectrochemical water splitting.

4. Experimental Section

Synthesis of α-$SnWO_4$ and NiO_x: PLD was used to deposit α-$SnWO_4$ thin films and NiO_x overlayers based on a previously published procedure,[17] and is briefly described below. Fluorine-doped tin oxide coated glass (FTO TEC 7, Pilkington) substrates were used as the transparent conductive back contact. Prior to deposition, the substrates (24×24 mm^2) were successively cleaned in an ultrasonic bath using a 1 vol% Triton solution (Triton X-100, laboratory grade, Sigma-Aldrich), acetone, isopropanol, ethanol, and deionized water for 15 min each. Afterwards they were dried under an N_2 stream.

Ablation of a ceramic α-$SnWO_4$ target was performed in a custom-built PLD system from PREVAC at room temperature equipped with a KrF-excimer laser with a wavelength of $\lambda = 248$ nm (LPXpro 210, Coherent). The base pressure of the deposition chamber was $\approx 1 \times 10^{-7}$ mbar. The laser fluence was adjusted to 2 J cm^{-2} with a laser spot size of 1.3×2 mm^2 and the repetition rate was 10 Hz. Film deposition was performed with an oxygen background pressure of $\approx 10^{-4}$ mbar. Substrates were fixed in an off-axis position with a target-to-substrate distance of 60 mm. A continuous substrate rotation of 12° s^{-1} was applied to achieve homogeneous films. Prior to every deposition a pre-ablation routine was performed to transform the target to a steady state condition, which was achieved when a constant deposition rate was monitored with a quartz crystal microbalance (QCM). Different film thicknesses were achieved by adjusting the respective number of laser shots. After deposition, the films were post-annealed in a tube furnace in Ar atmosphere at 520 °C for 2 h to prevent film oxidation. The presence of oxygen was minimized by evacuating the tube and flushing with Ar twice before annealing.

NiO_x was deposited by ablating a metallic Ni target in the same PLD system. The process was done at room temperature under an oxygen background pressure of 0.05 mbar. The laser fluence was 2 J cm^{-2} and a repetition rate of 10 Hz was used.

Characterization: X-ray diffraction was performed with a Bruker D8 Advance diffractometer in a grazing incidence configuration with a grazing incidence angle of 0.5°. The step size was set to 0.02° and the respective integration time per step was 6 s. Cu Kα ($\lambda = 1.5406$ Å) was used as the X-ray source with a voltage of 40 kV and a current of 40 mA.

Photoelectrochemistry (PEC) measurements were performed in a three-electrode configuration in a custom-made PEC cell. The sample was connected as the working electrode to an EG&G Princeton Applied Research (Model 273A) potentiostat. A platinum wire was used as the counter electrode, and an Ag/AgCl electrode (XR300, saturated KCl, Radiometer Analytical) was used as the reference electrode. Measured potentials were translated to the RHE by using the Nernst equation. AM1.5 illumination was obtained with a WACOM Super Solar Simulator (Model WXS-505-5H, AM1.5, Class AAA). The used electrolyte was 0.5 M potassium phosphate buffer (KP_i, pH 7.2) made from dissolving KH_2PO_4 (≥99.0%, Sigma-Aldrich) and K_2HPO_4 (≥99.0%, Sigma-Aldrich) with a 1:1.4 molar ratio in Milli-Q water. As a hole scavenger, 0.5 M Na_2SO_3 was added to the buffer solution. OCP measurements were performed under the same conditions.

HAXPES was performed at the Bessy II synchrotron facility at Helmholtz-Zentrum Berlin, Germany. Measurements were performed at the high kinetic energy photoemission end station (HIKE)[42] at the KMC-1 beamline.[43] During the measurements the analysis chamber was kept at $\approx 10^{-8}$ mbar. Photon energies were varied between 2003, 4000, and 6009 eV using the Si (111) and Si (311) cut crystals pairs of a double crystal monochromator. Photoelectrons were detected by a Scienta R4000 analyzer. Survey spectra were recorded with a step size of 0.5 eV and a pass energy of 200 eV. Core level and valence band spectra were recorded with a step size of 0.05 eV and a pass energy of 200 eV. Binding energies were referenced to the Au 4f core level (binding energy set equal to 84.00 eV) measured on a gold foil located on the sample manipulator which shared a common ground with the sample and the analyzer; in order to extract the binding energies and the contribution of the respective oxidation states from measured spectra a fitting procedure was applied. Before that a Shirley baseline subtraction was performed. The peak shape was represented by pseudo-Voigt functions consisting of a convolution of Gaussian and Lorentzian functions. Finally, chi-square minimization was performed to optimize the fitted spectra.

TEM was performed using a Philips CM12/STEM. The system is equipped with a LaB_6 cathode and a super twin lens for high resolution. An acceleration voltage of 120 keV was used. Four preparation samples were cut into small pieces and polished from both sides until reaching a thickness of 4–6 µm. Afterwards a Mo ring was glued on the sample. The samples were further thinned with an Ar ion mill until they had electron transparent areas.

Density Functional Theory: Starting from the $2 \times 1 \times 2$ supercell model, which includes 16 functional units of $Sn_{16}W_{16}O_{64}$ or 96 atoms of the orthorhombic crystal lattice of α-$SnWO_4$ (*Pnna* space group),[18,19,22–24] a perfect lattice and five representative self-defective lattices containing intrinsic O-, Sn-, and W-vacancies as well as Sn-antisite on W and W-antisite on Sn were modeled to mimic the possible presence of Sn^{4+} in α-$SnWO_4$ samples. For O-, Sn-, and W-deficient α-$SnWO_4$, one O atom, one Sn-atom, and one W atom were removed from the $Sn_{16}W_{16}O_{64}$ supercell, respectively. For Sn-antisite on W, one W-atom was replaced by one Sn-atom in the $Sn_{16}W_{16}O_{64}$ supercell. For W-antisite on Sn, one Sn-atom was replaced by one W-atom in the $Sn_{16}W_{16}O_{64}$ supercell. For each defect type, different spin multiplicities were explored in order to come up with the most stable spin configuration.

The various generated crystalline structures were fully optimized by means of the spin-polarized DFT using the Vienna Ab initio simulation package (VASP)[44–46] with the Perdew–Burke–Ernzerhof (PBE) exchange correlation potential[47] and the frozen-core projector augmented-wave (PAW) approach.[48] The configurations of valence electrons treated explicitly in the plane wave descriptions are $5s^25p^2$ for Sn, $5d^46s^2$ for W, and $2s^22p^4$ for O. Upon several benchmark tests evaluating the accuracy of the calculations, a kinetic cutoff energy of 400 eV was consistently used for electron wave functions expansion and a Monkhorst–Pack *k*-point mesh[49] of $3 \times 3 \times 3$ was used for sampling the Brillion zone. Gaussian smearing was used with a sigma value of 0.1 eV. The atomic positions were fully relaxed with the conjugate gradient procedure until the residual forces vanished within 0.01 eV Å^{-1} and the electronic convergence for each supercell was below 10^{-6} eV. Our PBE-based computed lattice parameters ($a = 5.59$ Å, $b = 11.63$ Å, $c = 4.98$ Å, and $\alpha = \beta = \gamma = 90°$) of the pristine material are in excellent agreement with the experimental values ($a = 5.62$ Å, $b = 11.74$ Å, $c = 4.98$ Å, and $\alpha = \beta = \gamma = 90°$).[17,22–24,50]

By considering the optimized geometries obtained with the PBE functional, the electronic structure calculations of pristine and the most relevant self-defective α-$SnWO_4$ materials were conducted at the level of the more expensive screened coulomb hybrid Heyd–Scuseria–Ernzerhof (HSE06)[51] functional using VASP. This method has been proven to provide much more accurate band gap values of a large number of photocatalytic semiconductors than the standard generalized-gradient approximation (GGA) functional.[52–58] The electronic properties analysis covered the DOS together with the partial charge density maps corresponding to the new states introduced by the created defects in terms of orbital contribution types of each element in the cell. The validity of our electronic structure calculation is demonstrated by the relatively good agreement between our HSE06-based computed band gap of 1.5 eV for the pristine material with the reported experimental values (in between 1.6 and 1.9 eV), which is much more accurate than the PBE computed one of 0.8 eV.[17,19,22–24]

Supporting Information

Supporting Information is available from the Wiley Online Library or from the author.

Acknowledgements

The authors acknowledge financial support for this work from the Helmholtz International Research School "Hybrid Integrated Systems for Conversion of Solar Energy" (HI-SCORE), an initiative co-funded by the Initiative and Networking Fund of the Helmholtz Association. Part of the work was funded by the Volkswagen Foundation. They would also like to thank Roberto Felix Duarte and Regan Wilks for the access and technical assistance to the HiKE endstation, KMC-1 beamline at the BESSY-II synchrotron facility, as well as Karsten Harbauer and Ronen Gottesman for supporting the PLD experiments. M.H. thanks the KAUST Supercomputing Laboratory for the needed computational resources. The authors thank Ulrike Bloeck for recording the TEM images.

Open access funding enabled and organized by Projekt DEAL.

Conflict of Interest

The authors declare no conflict of interest.

Data Availability

The data that support the findings of this study are available from the corresponding author upon reasonable request.

Keywords

DFT, HAXPES, interface, photovoltage, pulsed laser deposition, α-$SnWO_4$

Received: October 6, 2020
Revised: December 27, 2020
Published online: January 14, 2021

[1] M. G. Walter, E. L. Warren, J. R. McKone, S. W. Boettcher, Q. Mi, E. A. Santori, N. S. Lewis, *Chem. Rev.* **2010**, *110*, 6446.
[2] M. Grätzel, *Nature* **2001**, *414*, 338.
[3] J. A. Turner, *Science* **2004**, *305*, 972.
[4] R. van de Krol, B. A. Parkinson, *MRS Energy Sustain.* **2017**, *4*, E13.
[5] S. Ardo, D. F. Rivas, M. A. Modestino, V. Schulze Greiving, F. F. Abdi, E. Alcaron Llado, V. Artero, K. Ayers, C. Battaglia, J.-P. Becker, D. Bederak, A. Berger, F. Buda, E. Chinello, B. Dam, V. Di Palma, T. Edvinsson, K. Fujii, H. Gardeniers, H. Geerlings, S. M. H. Hashemi, S. Haussener, F. Houle, J. Huskens, G. F. Morre, J. Muller, K. L. Orchard, T. E. Rosser, F. H. Saadi, J.-W. Schüttauf, B. Seger, S. W. Sheehan, W. A. Smith, J. Spurgeon, M. H. Tang, R. van de Krol, P. C. K. Vesborg, P. Westerik, *Energy Environ. Sci.* **2018**, *11*, 2768.
[6] D. K. Lee, D. Lee, M. A. Lumley, K.-S. Choi, *Chem. Soc. Rev.* **2019**, *48*, 2126.
[7] F. F. Abdi, S. P. Berglund, *J. Phys. D: Appl. Phys.* **2017**, *50*, 193002.
[8] K. Sivula, R. van de Krol, *Nat. Rev. Mater.* **2016**, *1*, 15010.
[9] K. Sivula, *J. Phys. Chem. Lett.* **2013**, *4*, 1624.
[10] O. Khaselev, J. A. Turner, *Science* **1998**, *280*, 425.
[11] J. L. Young, M. A. Steiner, H. Döscher, R. M. France, J. A. Turner, T. G. Deutsch, *Nat. Energy* **2017**, *2*, 17028.
[12] M. M. May, H.-J. Lewerenz, D. Lackner, F. Dimroth, T. Hannappel, *Nat. Commun.* **2015**, *6*, 8286.
[13] M. J. Kenney, M. Gong, Y. Li, J. Z. Wu, J. Feng, M. Lanza, H. Dai, *Science* **2013**, *342*, 836.
[14] T. W. Kim, K.-S. Choi, *Science* **2014**, *343*, 990.
[15] Y. Pihosh, I. Turkevych, K. Mawatari, J. Uemura, Y. Kazoe, S. Kosar, K. Makita, T. Sugaya, T. Matsui, D. Fujita, M. Tosa, M. Kondo, T. Kitamori, *Sci. Rep.* **2015**, *5*, 11141.
[16] A. Kudo, K. Omori, H. Kato, *J. Am. Chem. Soc.* **1999**, *121*, 11459.
[17] M. Kölbach, I. J. Pereira, K. Harbauer, P. Plate, K. Höflich, S. P. Berglund, D. Friedrich, R. van de Krol, F. F. Abdi, *Chem. Mater.* **2018**, *30*, 8322.
[18] M. Kölbach, H. Hempel, K. Harbauer, M. Schleuning, A. Petsiuk, K. Höflich, V. Deinhart, D. Friedrich, R. Eichberger, F. F. Abdi, R. van de Krol, *ACS Appl. Energy Mater.* **2020**, *3*, 4320.
[19] K. J. Pyper, T. C. Evans, B. M. Bartlett, *Chin. Chem. Lett.* **2015**, *26*, 474.
[20] F. Bozheyev, E. M. Akinoglu, L. Wu, H. Lu, R. Nemkayeva, Y. Xue, M. Jin, M. Giersig, *Int. J. Hydrog. Energy* **2020**, *45*, 8676.
[21] M. Harb, A. Ziani, K. Takanabe, *Phys. Status Solidi B* **2016**, *253*, 1115.
[22] A. Ziani, M. Harb, D. Noureldine, K. Takanabe, *APL Mater.* **2015**, *3*, 096101.
[23] Z. Zhu, P. Sarker, C. Zhao, L. Zhou, R. L. Grimm, M. N. Huda, P. M. Rao, *ACS Appl. Mater. Interfaces* **2017**, *9*, 1459.
[24] I. Cho, C. H. Kwak, D. W. Kim, S. Lee, K. S. Hong, *J. Phys. Chem. C* **2009**, *113*, 10647.
[25] B. Klahr, T. Hamann, *J. Phys. Chem. C* **2014**, *118*, 10393.
[26] M. S. Prévot, X. A. Jeanbourquin, W. S. Bourée, F. F. Abdi, D. Friedrich, R. van de Krol, N. Guijarro, F. Le Formal, K. Sivula, *Chem. Mater.* **2017**, *29*, 4952.
[27] B. A. De Angelis, M. Schiavello, *J. Solid State Chem.* **1977**, *21*, 67.
[28] R. Irani, P. Plate, C. Höhn, P. Bogdanoff, M. Wollgarten, K. Höflich, R. van de Krol, F. F. Abdi, *J. Mater. Chem. A* **2020**, *8*, 5508.
[29] Y. Hermans, S. Murcia-López, A. Klein, R. van de Krol, T. Andreu, J. R. Morante, T. Toupance, W. Jaegermann, *Phys. Chem. Chem. Phys.* **2019**, *21*, 5086.
[30] D. Bae, B. Seger, P. C. K. Vesborg, O. Hansen, I. Chorkendorff, *Chem. Soc. Rev.* **2017**, *46*, 1933.
[31] I. A. Digdaya, G. W. P. Adhyaksa, B. J. Trzesniewski, E. C. Garnett, W. A. Smith, *Nat. Commun.* **2017**, *8*, 15968.
[32] H.-J. Lewerenz, *J. Electroanal. Chem.* **1993**, *365*, 121.
[33] A. J. Bard, A. B. Bocarsly, F. F. Fan, E. G. Walton, M. S. Wrighton, *J. Am. Chem. Soc.* **1980**, *102*, 3671.
[34] S. W. Lee, Y. S. Lee, J. Heo, S. C. Siah, D. Chua, R. E. Brandt, S. B. Kim, J. P. Mailoa, T. Buonassisi, R. G. Gordon, *Adv. Energy Mater.* **2014**, *4*, 1301916.
[35] J. Lu, J. Aarik, J. Sundqvist, K. Kukli, A. Hårsta, J. O. Carlsson, *J. Cryst. Growth* **2005**, *273*, 510.
[36] X. Ding, X. Wang, Y. Feng, W. Shen, L. Liu, *Jpn. J. Appl. Phys.* **2020**, *59*, SGGB16.
[37] A. Kuzmin, M. Zubkins, R. Kalendarev, *Ferroelectrics* **2015**, *484*, 49.
[38] I. J. McColm, R. Steadman, A. Howe, *J. Solid State Chem.* **1970**, *2*, 555.
[39] Materials Project, https://www.osti.gov/servlets/purl/1322198 (accessed: December 2020).
[40] W. Smekal, W. S. M. Werner, C. J. Powell, *Surf. Interface Anal.* **2005**, *37*, 1059.
[41] S. Gates-Rector, T. Blanton, *Powder Diffr.* **2019**, *34*, 352.
[42] M. Gorgoi, S. Svensson, F. Schäfers, G. Öhrwall, M. Mertin, P. Bressler, O. Karis, H. Siegbahn, A. Sandall, H. Rensmo, W. Doherty, C. Jung, W. Braun, W. Eberhardt, *Nucl. Instrum. Methods Phys. Res., Sect. A* **2009**, *601*, 48.
[43] F. Schaefers, M. Mertin, M. Gorgoi, *Rev. Sci. Instrum.* **2007**, *78*, 123102.
[44] G. Kresse, J. Furthmüller, *Comput. Mater. Sci.* **1996**, *6*, 15.
[45] G. Kresse, J. Furthmüller, *Phys. Rev. B* **1996**, *54*, 11169.
[46] G. Kresse, J. Hafner, *Phys. Rev. B* **1994**, *49*, 14251.
[47] J. P. Perdew, K. Burke, M. Ernzerhof, *Phys. Rev. Lett.* **1996**, *77*, 3865.
[48] P. E. Blöchl, *Phys. Rev. B* **1994**, *50*, 17953.
[49] H. J. Monkhorst, J. D. Pack, *Phys. Rev. B* **1976**, *13*, 5188.

[50] A. Kuzmin, A. Anspoks, A. Kalinko, J. Timoshenko, R. Kalendarev, *Sol. Energy Mater. Sol. Cells* **2015**, *143*, 627.
[51] J. Heyd, G. E. Scuseria, *J. Chem. Phys.* **2003**, *118*, 8207.
[52] M. Harb, L. Cavallo, *ACS Omega* **2018**, *3*, 18117.
[53] S. Lardhi, L. Cavallo, M. Harb, *J. Phys. Chem. C* **2018**, *122*, 18204.
[54] S. Lardhi, A. Curutchet, L. Cavallo, M. Harb, T. Le Bahers, *Phys. Chem. Chem. Phys.* **2017**, *19*, 12321.
[55] D. Noureldine, S. Lardhi, A. Ziani, M. Harb, L. Cavallo, K. Takanabe, *J. Mater. Chem. C* **2015**, *3*, 12032.
[56] M. Harb, D. Masih, S. Ould-Chikh, P. Sautet, J.-M. Basset, K. Takanabe, *J. Phys. Chem. C* **2013**, *117*, 17477.
[57] M. Harb, P. Sautet, E. Nurlaela, P. Raybaud, L. Cavallo, K. Domen, J.-M. Basset, K. Takanabe, *Phys. Chem. Chem. Phys.* **2014**, *16*, 20548.
[58] M. Harb, P. Sautet, P. Raybaud, *J. Phys. Chem. C* **2011**, *115*, 19394.